



Growth of nickel (111) plane: The key role in nickel for further improving the electrochemical property of hexagonal nickel hydroxide-nickel & reduced graphene oxide composite



Jinglin Zhang ^{a,1}, Huidi Liu ^{a,1}, Pu Shi ^a, Yaoji Li ^a, Langhuan Huang ^a, Wenjie Mai ^b, Shaozao Tan ^{a,*}, Xiang Cai ^c

^a Department of Chemistry, Jinan University, Guangzhou 510632, PR China

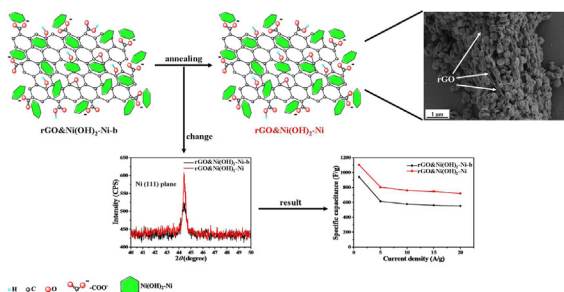
^b Department of Physics, Jinan University, Guangzhou 510632, PR China

^c Department of Light Chemical Engineering, Guangdong Polytechnic, Foshan 528041, PR China

HIGHLIGHTS

- A reduced graphene oxide and $\text{Ni(OH)}_2/\text{Ni}$ ($\text{rGO}\&\text{Ni(OH)}_2\text{-Ni}$) composite is got easily.
- The existence of Ni can enhance the thermal stability of Ni(OH)_2 .
- The coexistence of rGO and Ni can greatly improve the electrical conductivity.
- The (111) plane plays a key role in Ni for improving the electrochemical activity.
- The $\text{rGO}\&\text{Ni(OH)}_2\text{-Ni}$ composite exhibits superior electrochemical property.

GRAPHICAL ABSTRACT



ARTICLE INFO

Article history:

Received 7 February 2014

Received in revised form

19 May 2014

Accepted 20 May 2014

Available online 2 June 2014

Keywords:

Reduced graphene oxide

Nickel hydroxide

Nickel

Plane

Supercapacitor

ABSTRACT

Hexagonal nickel hydroxide/nickel decorated on reduced graphene oxide ($\text{rGO}\&\text{Ni(OH)}_2\text{-Ni}$) has been prepared via easy one-step chemical precipitation method and subsequent annealing treatment. The results show that the thermal stability of Ni(OH)_2 is enhanced by the incorporation of Ni. Besides, hexagonal $\text{Ni(OH)}_2\text{-Ni}$ nanoplate which can supply a short diffusion and migration pathway for electron and electrolyte ion contacts closely with the surface of rGO, resulting that the agglomeration of rGO is effectively prevented. Due to the good electrical conductivity of Ni, the incorporation of Ni can also improve the electrical conductivity of Ni(OH)_2 . More importantly, the Ni (111) plane is grown after annealing treatment, which plays a key role in Ni for further improving the electrochemical activity of composite. Consequently, the $\text{rGO}\&\text{Ni(OH)}_2\text{-Ni}$ electrode exhibits high capacitance, high energy density, excellent rate capability, good cycle stability, etc. The advantages of easy preparation and excellent electrochemical performance imply the great potential application of $\text{rGO}\&\text{Ni(OH)}_2\text{-Ni}$ in supercapacitors. Moreover, it is worthy noting that this work will offer a new approach for using metal nanoparticle in improving the electrochemical property of supercapacitor electrode material.

Crown Copyright © 2014 Published by Elsevier B.V. All rights reserved.

* Corresponding author. Tel./fax: +86 20 85223670.

E-mail address: tanshaozao@163.com (S. Tan).

¹ These authors contributed equally to this work.

1. Introduction

Supercapacitors, one of the new and promising energy storage and conversion devices, have attracted tremendous attention owing to higher energy density than that of conventional dielectric capacitors, larger power density and longer cycle life than those of batteries, low self-discharging, low maintenance cost and environmental friendliness [1–4]. Nowadays, supercapacitors have found extensive applications, including industrial power, mobile electrical system, portable consumer electronics, power and memory back-up system, etc [5,6]. Generally speaking, supercapacitors store energy based on two types of mechanisms: fast surface redox reaction (pseudocapacitors) and ion adsorption (electrochemical double layer capacitors, EDLCs) [7]. Unfortunately, the specific capacitance of EDLCs is usually low, which can not meet the ever-increasing need for some fields where high energy density is a key requirement. Therefore, using pseudocapacitive materials for supercapacitors has caused much interest since the energy density associated with Faradaic reaction is substantially higher by at least one order of magnitude than that of EDLCs [1,8–14].

Pseudocapacitive materials mainly contain metal oxides/hydroxides and conductive polymers, which are capable of rich redox reaction because of multiple oxidation states/structures. Among them, nickel hydroxide (Ni(OH)_2) is a promising candidate for supercapacitors due to its high theoretical specific capacitance (ca. 3750 F g^{-1}), well-defined electrochemical redox activity, low cost and easy synthesis [15]. It is noteworthy that the specific capacitance of Ni(OH)_2 , which may depend on its structure and morphology, is usually lower than its theoretical value. Thus, many established methods are used to synthesize nano-sized Ni(OH)_2 with various architectures (e.g., flower, flake and plate) to obtain improved electrochemical performance [16–18]. Nevertheless, the major issue of Ni(OH)_2 used as electrode for supercapacitors is its poor electrical conductivity, which can not make Ni(OH)_2 meet fast electron transport under high-rate charge and discharge, resulting in the compromises of rate capability and reversibility. For solving this predicament, considerable research efforts have been carried out, where Ni(OH)_2 is usually mixed with highly conductive carbon materials, such as carbon nanotube [19], graphene [20,21] and mesoporous carbon [22].

Graphene, a single-atom-thick two-dimensional graphitic carbon material, has attracted multidisciplinary attention thanks to its high electrical conductivity, large surface area and good chemical stability [23,24]. In recent years, extensive studies have developed the graphene-based materials for supercapacitors [25,26]. The results of these studies show improved electrochemical performance, because the advantages of each component can be combined and the special properties may be offered by the reinforcement or modification of each other. However, due to the strong Van der Waals interaction, graphene sheets usually suffer from serious agglomeration or re-stacking during fabrication process, which will lead to great loss of its excellent property. Consequently, the capacitive behavior of graphene-based material is much lower than the expected value in practical application. On the other hand, some researchers have reported that nickel ion in the Ni(OH)_2 lattice is partially substituted by other metal ions (e.g., Co [27], Zn [28] and Al [29]) or Ni(OH)_2 is mixed with non-carbon materials like metal oxide (e.g., Co_3O_4 [30]) and metal nanoparticle (e.g., Ag [31]). These research results also show the enhanced electrochemical property, which may be due to the synergistic effect among individual components that can improve electron and ion conduction, chemical stability and mechanical stability as well as pseudocapacitance.

In this paper, we propose an advanced electrochemical pseudocapacitive material based on reduced graphene oxide and nickel hydroxide/nickel ($\text{rGO}\&\text{Ni(OH)}_2\text{-Ni}$) via easy one-step chemical precipitation method and subsequent annealing treatment. First, the carboxyl of graphene oxide (GO) is mostly ionized through absorbing thermal energy when the GO solution is heated, which causes added negative charge of the GO surface, resulting that a great deal of Ni^{2+} can be adsorbed and enriched on the surface of GO. As a result, the reduction of GO and the generations of Ni(OH)_2 and Ni are achieved simultaneously with the assistance of hydrazine hydrate ($\text{N}_2\text{H}_4\cdot\text{H}_2\text{O}$). The results show that the existence of Ni can enhance the thermal stability of Ni(OH)_2 . Besides, Ni(OH)_2 is mixed with Ni to form hexagonal nanoplate that can provide a short diffusion and migration pathway for electron and electrolyte ion. Such hexagonal $\text{Ni(OH)}_2\text{-Ni}$ nanoplate closely contacts on the surface of rGO, resulting that the agglomeration of rGO is effectively prevented. In addition, the coexistence of rGO and Ni can much better improve the electrical conductivity of Ni(OH)_2 than the single existence of rGO, thanks to the good electrical conductivity of Ni. More importantly, the (111) plane of Ni is grown after annealing treatment, which plays a key role in Ni for further improving the electrochemical activity of composite. Consequently, the $\text{rGO}\&\text{Ni(OH)}_2\text{-Ni}$ composite exhibits excellent electrochemical properties, including high capacitance, high energy density, excellent rate capability, good cycle stability, etc. The advantages combining easy preparation and remarkable electrochemical performance suggest the great potential application of $\text{rGO}\&\text{Ni(OH)}_2\text{-Ni}$ in supercapacitors. Moreover, the synthesis developed in this work will offer a new approach for using metal nanoparticle in improving the electrochemical property of supercapacitor electrode material.

2. Experimental section

2.1. Materials

Graphite powder (spectral pure) was purchased from Sino-pharm Chemical Reagent Co., Ltd. Nickel nitrate hexahydrate ($\text{Ni}(\text{NO}_3)_2\cdot 6\text{H}_2\text{O}$) was purchased from Jinhuada Chemical Reagent Co., Ltd (Guangzhou, China). Hydrazine hydrate (80%) was supplied by Fuyu Chemical Reagent Co., Ltd (Tianjin, China). All other reagents and solvents were obtained from commercial suppliers. All aqueous solutions were prepared with ultrapure water ($>18 \text{ M}\Omega$) from a Milli-Q Plus system (Millipore).

2.2. Synthesis of sample

GO was prepared by oxidizing natural graphite powder based on a modified Hummers method as originally presented by Kovtyukhova and colleagues [32,33]. The as-prepared GO was dispersed in deionized water (1 mg mL^{-1}) under ultrasonication and the homogeneous solution was placed in a water bath at 90°C for 14 h. The resulting product was washed with deionized water until $\text{pH} = 7$ and was dispersed again in deionized water. Afterwards, 5 g of nickel (II) nitrate hexahydrate was added into the above solution and the mixture was ultrasonicated for 0.5 h. Then, 20 mL 80% hydrazine hydrate was added in and the mixture was reacted at 95°C for 2 h. The obtained product was washed with deionized water until $\text{pH} = 7$ and was freeze-dried. Such acquired powder was designated as $\text{rGO}\&\text{Ni(OH)}_2\text{-Ni-b}$. Finally, the powder was further annealed in nitrogen atmosphere at 300°C for 2 h in a tube furnace and the product was designated as $\text{rGO}\&\text{Ni(OH)}_2\text{-Ni}$. Similarly, rGO was prepared according to the same method without the addition of nickel (II) nitrate hexahydrate and the annealing treatment.

2.3. Characterizations

X-ray diffraction (XRD) patterns were recorded on a diffractometer (D/max-1200) using graphite monochromatic Cu $K\alpha$ radiation ($\lambda = 0.1541$ nm) at a generator voltage of 40 kV and a current of 40 mA; measurements were conducted within a 2θ range of 5.0–80.0° at a scanning rate of 4°/min. Fourier transform infrared (FTIR) spectra between 400 and 4000 cm⁻¹ were obtained on a Nicolet 6700 spectrometer. X-ray photoelectron spectroscopy (XPS) spectrum was recorded by an ESCALAB 250 X-ray photoelectron spectroscopy (Thermo-VG Scientific). Thermogravimetric analysis (TGA) was run on an SDT Q600 V20.9 Build 20 thermogravimetric analyzer at a heating rate of 10 °C min⁻¹ from 30 to 800 °C in nitrogen flow. The chemical compositions of the samples were also analyzed by energy dispersive X-ray spectrometer (EDX) (Oxford ISIS-300). Field emission scanning electron microscopy (FESEM) images were performed on ZEISS field emission scanning electron microscope; the samples were coated with a thin layer of gold before analysis. Transmission electron microscopy (TEM) images were observed by using a JEOL JEM-2100F field emission transmission electron microscope.

2.4. Electrochemical measurements

The fabrication of working electrode was carried out as follows. The electroactive material, carbon black and polytetrafluoroethylene were mixed with ethanol in a mass ratio of 75:15:10. Then, the resulting slurry was pressed onto the nickel foam substrate (1 cm × 1 cm) and dried at 80 °C for 24 h. Finally, the electrode was pressed under a pressure of 20 Mpa. All electrochemical measurements were done in a three-electrode setup: Ni foam coated with electroactive material, nickel electrode and saturated calomel electrode (SCE) were the working electrode, counter electrode and reference electrode, respectively. The measurements were carried out in 6 mol L⁻¹ KOH aqueous electrolyte at room temperature. Cyclic voltammetry (CV) tests, galvanostatic charge and discharge (GCD) curves and electrochemical impedance spectroscopy (EIS) measurement were measured by an IVIUMSTAT electrochemical workstation (Holland). Therein, CV tests were recorded between -0.1 and 0.5 V (vs. SCE) at different scan rates, GCD curves were measured in the potential range of -0.05–0.40 V (vs. SCE) at different current densities, and EIS measurements were carried out at frequency range from 0.1 Hz to 10⁴ Hz with potential amplitude of 10 mV.

3. Results and discussion

3.1. Characterizations of structure and chemical composition

Fig. 1 (a) shows the XRD patterns of GO, rGO, rGO&Ni(OH)₂–Ni-b and rGO&Ni(OH)₂–Ni.

For GO, the peak of graphite at $2\theta = 26.4^\circ$ can not be observed while a new peak centered at $2\theta = 9.3^\circ$ appears which corresponds with the (002) interlayer spacing of 0.950 nm, revealing the successful oxidation of the original graphite. In the XRD pattern of rGO, the peak at $2\theta = 9.3^\circ$ disappears and a broad diffraction peak is observed at ~25° which is very close to that of pristine graphite, implying that the π -conjugated structure is recovered from GO upon chemical reduction and the framework of the reduced sample is re-stacked during the reduction process due to Van der Waals force [34]. For rGO&Ni(OH)₂–Ni-b, the characteristic diffraction peaks at $2\theta = 19.2^\circ$, 32.9°, 38.4°, 58.8°, 62.6°, 70.4° and 72.8° are found, corresponding to the (001), (100), (101), (110), (111), (103) and (201) reflections of β -Ni(OH)₂ [35]. Moreover, some diffraction peaks at $2\theta = 44.5^\circ$, 51.9° and 76.4° are also observed, which respectively coincide with the (111), (200) and (220) planes of nickel according to a standard PDF card (No. 04-0850). These results indicate that Ni(OH)₂ and Ni are synthesized at the same time under the reaction condition. Generally, Ni(OH)₂, even though it is combined with rGO, can be transformed into NiO under annealing treatment (e.g., our experiment condition) [36–38]. However, to our surprise, no diffraction peaks belonging to NiO can be observed and all diffraction peak locations of rGO&Ni(OH)₂–Ni are as same as those of rGO&Ni(OH)₂–Ni-b in the XRD pattern of rGO&Ni(OH)₂–Ni. Moreover, the intensity of diffraction peak belonging to the Ni (111) plane is increased after annealing treatment (**Fig. 1(b)**). These results indicate that Ni may be able to improve the thermal stability of Ni(OH)₂ through absorbing heat energy from annealing treatment, resulting in the growth of Ni (111) plane instead of the decomposition of Ni(OH)₂. On the other hand, the diffraction peak for rGO can not be observed in the XRD pattern of rGO&Ni(OH)₂–Ni-b or rGO&Ni(OH)₂–Ni, owing to more disordered stacking and quite uniform dispersion of rGO caused by the incorporation of Ni(OH)₂–Ni.

In order to further confirm that Ni(OH)₂ is not decomposed after annealing treatment, the composition and chemical structure of sample are analyzed by XPS and FTIR spectroscopy. In the XPS survey spectrum of rGO&Ni(OH)₂–Ni (**Fig. 2 (a)**), it shows that the composite mainly consists of carbon, oxygen and nickel species.

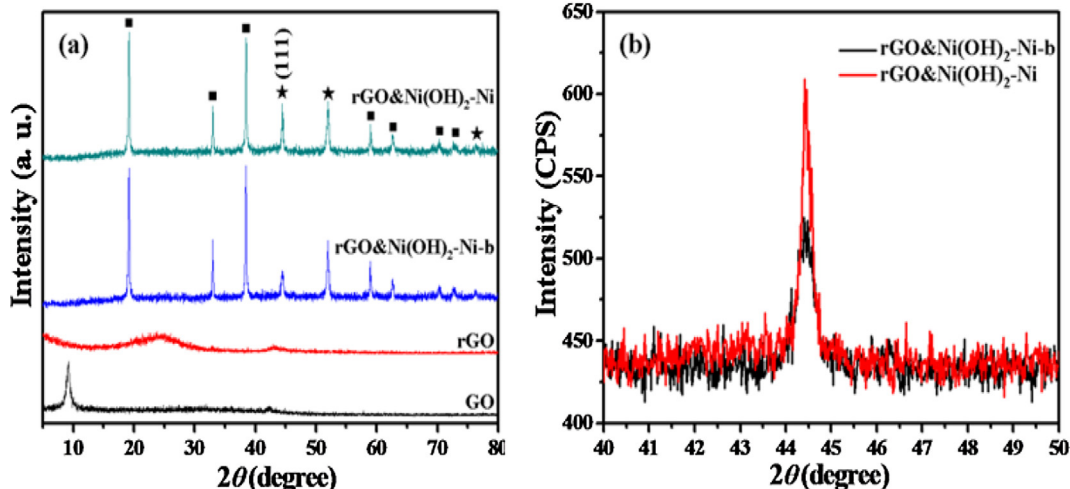


Fig. 1. (a) XRD patterns of GO, rGO, rGO&Ni(OH)₂–Ni-b and rGO&Ni(OH)₂–Ni. (b) XRD patterns of Ni (111) plane of rGO&Ni(OH)₂–Ni-b and rGO&Ni(OH)₂–Ni.

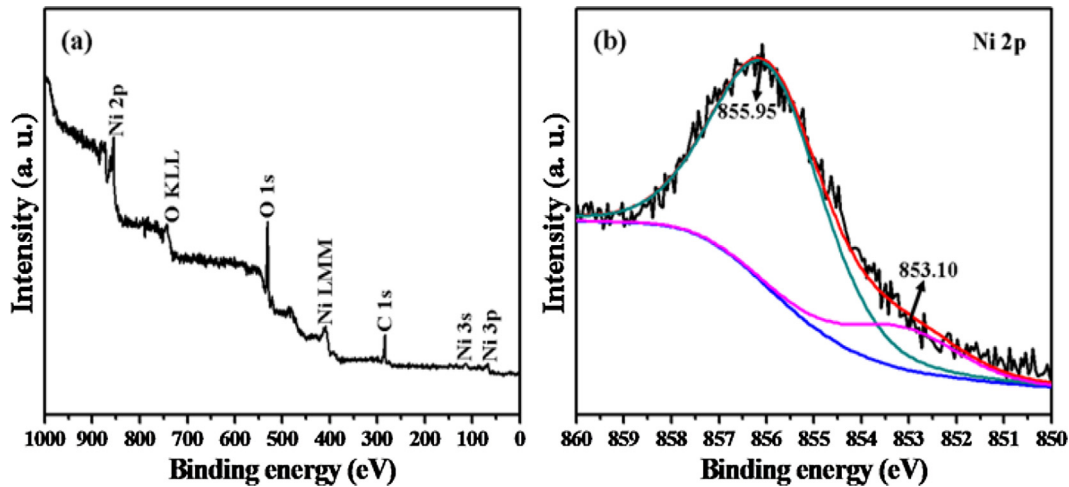


Fig. 2. (a) XPS survey spectrum of rGO&Ni(OH)₂-Ni. (b) Ni 2p XPS spectrum of rGO&Ni(OH)₂-Ni.

The peak at 284.81 eV is ascribed to the characteristic peak of C 1s, which can be divided into several peaks (Fig. S1): C=C (284.75 eV) of sp² carbon in the basal plane of rGO, the carbon in C—O (286.10 eV), the carbonyl carbon in C=O (286.90 eV) and the carboxylate carbon in O—C=O (288.40 eV) [39,40], indicating that there are still some residual oxygen-containing groups on the surface of rGO due to the incomplete reduction. Besides, the Ni 2p XPS spectrum in Fig. 2(b) can be also divided into two peaks at 853.10 and 855.95 eV, corresponding to metallic nickel and Ni²⁺ in Ni(OH)₂, respectively [41,42]. This result demonstrates that Ni(OH)₂ is not decomposed at all after annealing treatment and coexists with Ni in rGO&Ni(OH)₂-Ni.

Fig. 3 shows the FTIR spectra of GO, rGO, rGO&Ni(OH)₂-Ni-b and rGO&Ni(OH)₂-Ni. For GO, a broad and intensive peak appeared at 3420 cm⁻¹ is assigned to O—H stretching band, which may originate from water molecules adsorbed inside GO. In addition, peaks at 1732, 1628, 1388 and 1051 cm⁻¹ respectively correspond to C=O, C=C, C—OH and C—O—C vibration frequencies, confirming the presences of various oxygen-containing functional groups in GO [43,44]. In contrast, the FTIR spectrum of rGO clearly shows that the intensities of peaks corresponding to various oxygen-containing functional groups are largely decreased, indicating

that GO has been successfully reduced. In the FTIR spectrum of rGO&Ni(OH)₂-Ni-b, a narrow and sharp peak at 3642 cm⁻¹ is ascribed to the O—H stretching vibration, which confirms the brucite structure of β-Ni(OH)₂ phase. Besides, the strong band at 550 cm⁻¹ corresponds with the Ni—O—H stretching vibration and the small weak peak centered around 458 cm⁻¹ is assigned to the Ni—O stretching mode [45,46]. For rGO&Ni(OH)₂-Ni, it can be seen that all peak locations remain unchanged compared with those of rGO&Ni(OH)₂-Ni-b, implying that Ni(OH)₂ is still present after annealing treatment. Since Ni is metal, no peaks belonging to Ni can be seen in the FTIR spectrum of rGO&Ni(OH)₂-Ni-b or rGO&Ni(OH)₂-Ni. The XPS and FTIR results are consistent with XRD analysis. Therefore, we can make a conclusion that Ni(OH)₂ and Ni are coexisted. Moreover, Ni(OH)₂ is not decomposed at all after annealing treatment, which is due to the introduction of Ni that may have the ability to improve the thermal stability of Ni(OH)₂.

So as to prove the hypothesis that Ni can improve the thermal stability of Ni(OH)₂, TGA is carried out. Fig. 4 shows the TGA curve of rGO&Ni(OH)₂-Ni-b performed from 30 to 800 °C in nitrogen flow at a heating rate of 10 °C min⁻¹. Obviously, the curve can be divided into three parts. The first weight loss is from 30 to 200 °C, which is mainly due to the evaporation of bounded water and some

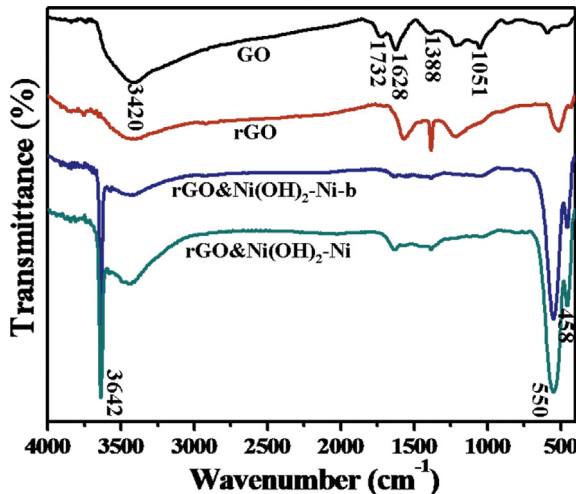


Fig. 3. FTIR spectra of GO, rGO, rGO&Ni(OH)₂-Ni-b and rGO&Ni(OH)₂-Ni.

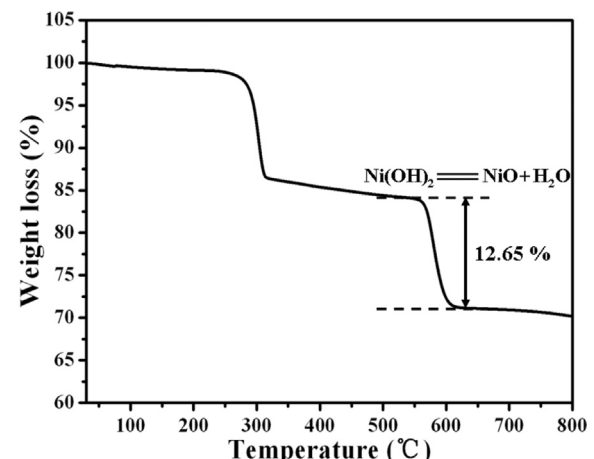


Fig. 4. TGA curve of rGO&Ni(OH)₂-Ni-b performed from 30 to 800 °C in nitrogen flow at a heating rate of 10 °C min⁻¹.

free water absorbed on the sample during the preparation process. The second weight loss near 240 °C is attributed to the decomposition of the residual oxygen-containing groups on the surface of rGO. The third weight loss above 550 °C is due to the decomposition of Ni(OH)₂. Generally speaking, the decomposition temperature of crystalline Ni(OH)₂ is 300 °C in nitrogen atmosphere [47]. However, in this work, we can find that the decomposition temperature of Ni(OH)₂ is increased greatly, indicating that the thermal stability of Ni(OH)₂ is improved. Since Ni(OH)₂ can be totally transformed into NiO at 300 °C even if it is combined with rGO [38], such improved thermal stability of Ni(OH)₂ is ascribed to the introduction of Ni. Some works have also reported that the addition of Ni can improve the thermal stability of material [48].

It is well known that Ni has good thermal conductivity as well as other metals. During annealing treatment at 300 °C, the thermal energy released in unit time is relatively few. Hence, the thermal energy is absorbed by Ni rather than is used for the decomposition of Ni(OH)₂, resulting in the growth of Ni (111) plane and the improvement of thermal stability of Ni(OH)₂. Nevertheless, too much thermal energy releases in unit time when the temperature increases to 550 °C. Subsequently, part of thermal energy begin to be absorbed by Ni(OH)₂, leading to the decomposition of Ni(OH)₂. Hence, we can make a conclusion that Ni can enhance the thermal stability of Ni(OH)₂.

From the XRD and XPS results of rGO&Ni(OH)₂–Ni, no diffraction peak belonging to NiO can be observed, indicating that Ni(OH)₂ is not decomposed after annealing treatment. We can know that the content of Ni(OH)₂ in rGO&Ni(OH)₂–Ni is the same as that in rGO&Ni(OH)₂–Ni-b. Therefore, the mass ratio of rGO to Ni(OH)₂–Ni and the one of Ni(OH)₂ to Ni species in rGO&Ni(OH)₂–Ni can be calculated based on the TGA curve of rGO&Ni(OH)₂–Ni-b and the XPS analysis of rGO&Ni(OH)₂–Ni. Specifically, from the TGA curve of rGO&Ni(OH)₂–Ni-b (Fig. 4), the third weight loss (12.65 wt.%) above 550 °C is ascribed to the decomposition of Ni(OH)₂. Based on this result, we can figure out the content of Ni(OH)₂ in rGO&Ni(OH)₂–Ni is 65.10 wt.% according to the reaction equation (Ni(OH)₂ = NiO + H₂O). Moreover, 44.52 wt.% nickel is estimated to be present in rGO&Ni(OH)₂–Ni based on the XPS result. Hence, we can calculate that the content of Ni in rGO&Ni(OH)₂–Ni is 3.310 wt.%. Finally, the remaining content is attributed to rGO (100 wt.%–3.310 wt.%–65.10 wt.% = 31.59 wt.%). From the above analysis, we can make a conclusion that the mass ratio of rGO, Ni(OH)₂ and Ni is 31.59: 65.10: 3.310.

3.2. Observation of morphology

The morphologies of the as-synthesized samples are investigated using FESEM. In Fig. 5 (a), the rGO shows sheet-like morphology with characteristically crumpled and rough architecture, and the layers of rGO are interacted with each other to form three-dimensional network. Fig. 5(b) shows the typical FESEM image of rGO&Ni(OH)₂–Ni-b, where a great number of hexagonal nanoplates appear. Moreover, the nanoplates are re-stacked to tightly contact and cover the rGO, leading the morphology of rGO can not be observed visibly. It should be noting that no other morphology can be seen except for the hexagonal nanoplate and the morphology of rGO, indicating that the hexagonal nanoplate is ascribed to the appearance of Ni(OH)₂–Ni. Compared with that of rGO&Ni(OH)₂–Ni-b, the FESEM image of rGO&Ni(OH)₂–Ni (Fig. 5(c,d)) shows the similar morphology where the average size of hexagonal nanoplates is 200 nm, revealing that annealing treatment has no obvious effect on the morphology of composite. Furthermore, EDX analysis (Fig. 5(e)) and Fig. S2 demonstrates that the rGO&Ni(OH)₂–Ni composite is primarily composed of elements Ni, C and O, which is in good agreement with XPS result. Other elements

like Si, Na, Al, Mg, Ca, P and Au are ascribed to the glass substrate and sputtered gold. From the EDX mapping analysis (Fig. 5(e)), it can be seen that element Ni is uniformly distributed, indicating that Ni(OH)₂–Ni is well distributed on the surface of rGO.

To further investigate the morphology of sample, TEM is also performed. In Fig. S3(a), the morphology of rGO is observed clearly, showing rGO is highly transparent with some visible wrinkles and ripples. For rGO&Ni(OH)₂–Ni-b (Fig. S3(b)), most of the rGO morphology is covered by some irregular hexagonal nanoplates which are ascribed to the appearance of Ni(OH)₂–Ni as described in FESEM. In addition, the black parts may be due to the re-stacking of Ni(OH)₂–Ni nanoplates. Moreover, the rGO&Ni(OH)₂–Ni (Fig. S3(c,d)) shows the similar morphology compared with rGO&Ni(OH)₂–Ni-b, which is the same as the results of FESEM. Observations from TEM images also indicate that the hexagonal Ni(OH)₂–Ni nanoplates closely contact with the surface of rGO. In order to prove that Ni combines with Ni(OH)₂ to form hexagonal nanoplate, high-resolution TEM images of hexagonal nanoplate in rGO&Ni(OH)₂–Ni are given (Fig. 6). The measured lattice space of 0.2064 nm is in good agreement with the *d*-spacing of (111) plane (0.2034 nm) of Ni, while the lattice spacing of 0.2324 nm well corresponds to the *d*-spacing of (101) plane (0.2342 nm) of Ni(OH)₂. Therefore, two kinds of lattice fringes can be observed, indicating that Ni and Ni(OH)₂ are coexisted in hexagonal nanoplate. Moreover, the lattice fringe of Ni(OH)₂ can be also found in the lattice fringe of Ni, implying that Ni has no fixed growing position in hexagonal nanoplate. Hence, we suggest that Ni mixed with Ni(OH)₂ is randomly distributed in the hexagonal nanoplate.

3.3. Exploration of formation mechanism

From the analyses above, the formation mechanism of rGO&Ni(OH)₂–Ni is suggested as follows (Fig. 7).

It is well known that the ionization of carboxyl is an endothermic reaction. Hence, the carboxyl on the surface of GO can be mostly ionized through absorbing thermal energy when the GO solution is heated at 90 °C for 14 h, resulting in added negative charge of the GO surface. On the other hand, Ni²⁺ is adsorbed on the surface of GO due to the electrostatic attraction between the Ni²⁺ and the negatively charged surface of GO. Therefore, more negative charge on the surface of GO will absorb more Ni²⁺ while the GO and Ni(NO₃)₂·6H₂O are mixed, causing a large number of Ni²⁺ are adsorbed and enriched on the surface of GO. Consequently, part of Ni²⁺ will react with reducing agent of N₂H₄·H₂O according to the reaction equation reported in other study [49], leading to the generation of Ni. Meanwhile, part of Ni²⁺ combines with OH[−] released from the decomposition of N₂H₄·H₂O to form Ni(OH)₂. As a result, the reduction of GO and the generations of Ni(OH)₂ and Ni are achieved simultaneously. During annealing treatment, Ni can improve the thermal stability of Ni(OH)₂ by absorbing the heat energy, resulting in the growth of Ni (111) plane instead of the decomposition of Ni(OH)₂. Thus, the chemical composition of composite remains unchanged after annealing treatment.

3.4. Investigation of electrochemical property

To explore the potential application, rGO&Ni(OH)₂–Ni is used as electrode material for supercapacitors and evaluated by electrochemical measurements in a three-electrode setup with 6 mol L^{−1} KOH aqueous electrolyte at room temperature.

Fig. 8 (a) shows the CV curves of rGO&Ni(OH)₂–Ni at scan rates ranging from 50 to 150 mV s^{−1} within the potential window of −0.1–0.5 V. It can be clearly observed that each of the CV curves exhibits a pair of strong redox current peaks, corresponding to the reversible Faradaic reaction between Ni (II) and Ni (III) [15]. In

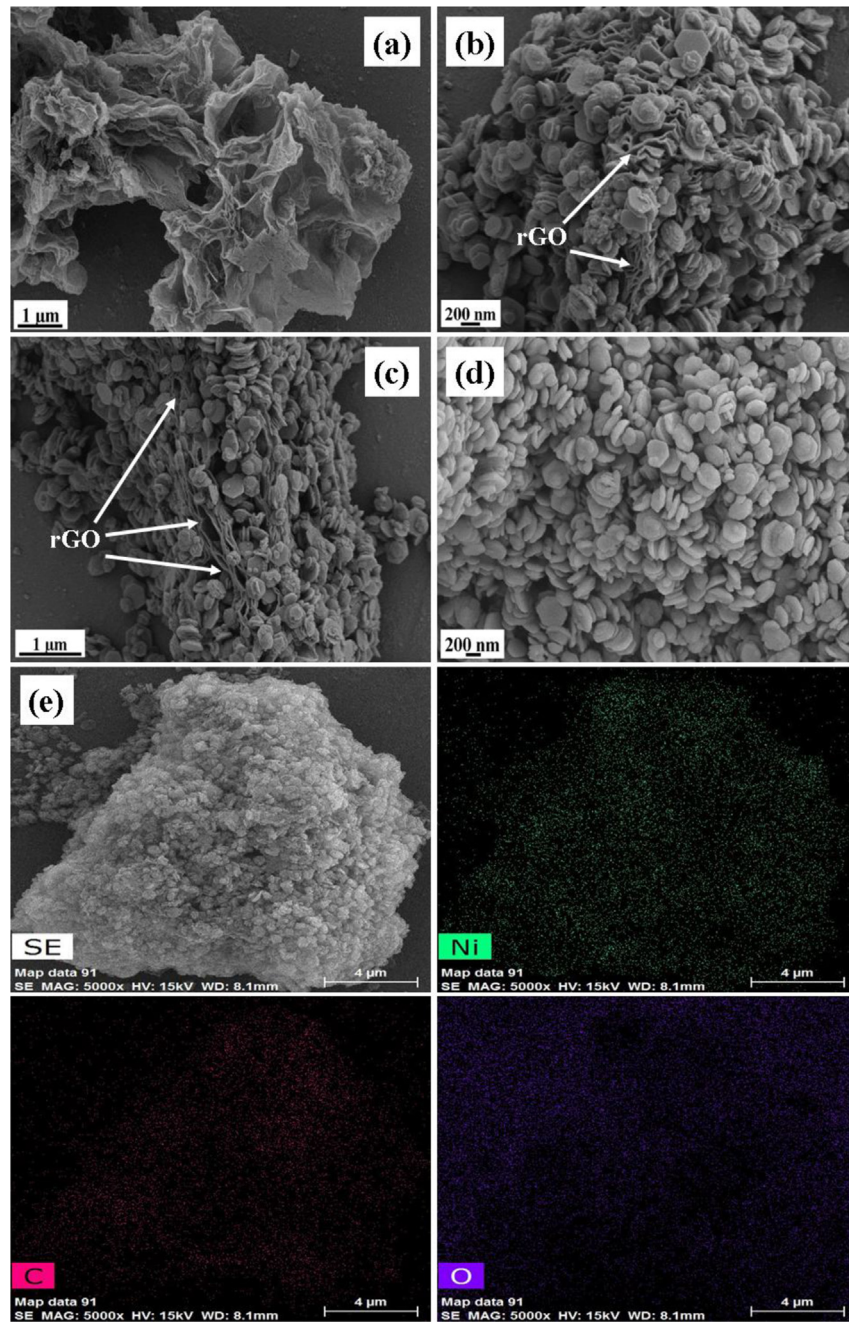


Fig. 5. FESEM images of (a) rGO, (b) rGO&Ni(OH)₂–Ni-b and (c,d) rGO&Ni(OH)₂–Ni. (e) EDX mapping analysis of rGO&Ni(OH)₂–Ni.

addition, the symmetric characteristic of anodic and cathodic peaks demonstrates the excellent reversibility of rGO&Ni(OH)₂–Ni electrode material. More importantly, the shapes of CV curves almost have no significant change at various scan rates, revealing that rGO&Ni(OH)₂–Ni electrode owns enhanced mass transportation and excellent electron conduction. Besides, slight shift of oxidation and reduction peaks can be found, which is probably caused by the internal resistance of electrode [50]. On the other hand, it can be seen in Fig. S4 that the difference between anodic peak and cathodic peak is approximately 110 mV. The difference ΔE_{OR} ($E_O - E_R$) between oxidation potential and reduction potential can be used to estimate the reversibility of the electrode reaction [51]. The smaller ΔE_{OR} value suggests the higher reversibility of the reaction. Comparing the ΔE_{OR} value in this work with those reported in other

studies (e.g., 120 mV for tubular Ni(OH)₂ and 180 mV for spherical powder) [51], the smaller ΔE_{OR} observed in this work also implies that rGO&Ni(OH)₂–Ni electrode has better reversibility of the electrochemical redox reaction.

GCD profile of rGO&Ni(OH)₂–Ni is shown in Fig. 8(b). Obviously, the rGO&Ni(OH)₂–Ni electrode exhibits typical pseudocapacitive behavior at various current densities, which corresponds with the CV result. Generally, the specific capacitance (C_s , F g⁻¹) can be calculated by the following equation:

$$C_s = \frac{It}{m\Delta V} \quad (1)$$

where I is the discharge current (A), t is the time for a full discharge (s), m is the mass of electroactive material (g), and ΔV is the

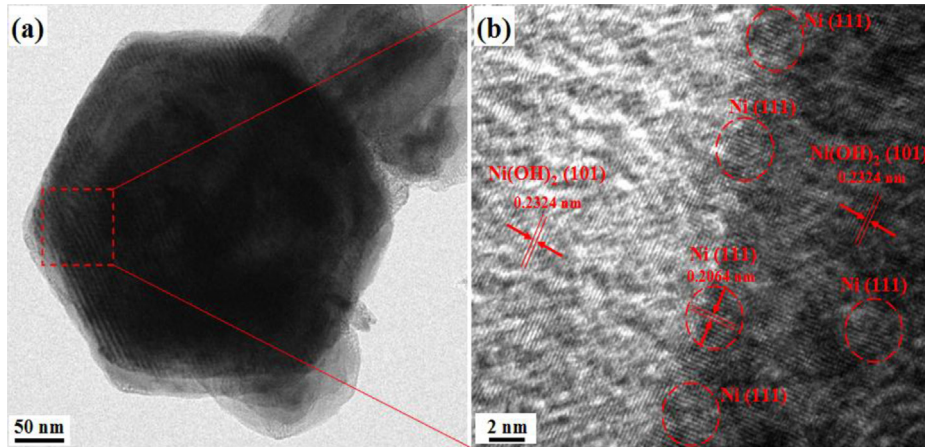


Fig. 6. (a,b) High-resolution TEM images of rGO&Ni(OH)₂–Ni.

potential range of a full discharge (V). Based on the total mass of sample, variation of C_s with current density for rGO&Ni(OH)₂–Ni electrode is given in Fig. 8(e). The highest C_s value of rGO&Ni(OH)₂–Ni is 1103 F g⁻¹ at current density of 1 A g⁻¹. With the increase of current density, the C_s is gradually decreased, which may be because some parts of the surface of rGO&Ni(OH)₂–Ni are not accessible at high charge and discharge rate. However, it is noteworthy that the C_s of rGO&Ni(OH)₂–Ni is still as high as 720 F g⁻¹ even at a high current density of 20 A g⁻¹. Approximate 65.28% of the initial C_s is retained with the current density increases from 1 to 20 A g⁻¹, revealing excellent rate capability of rGO&Ni(OH)₂–Ni which is quite crucial for the supercapacitor electrode material to achieve high energy density and power density. Remarkably, as shown in Table 1, the C_s value of rGO&Ni(OH)₂–Ni in this work is highly comparable with and even much higher than those of composites based on graphene and Ni(OH)₂ in other studies [15,21,50,52–54] and those of composites based on Ni(OH)₂ and other materials [19,31,55,56].

Moreover, the cycle life is tested by CV technique at a scan rate of 100 mV s⁻¹. The result (Fig. 8(c)) exhibits good cycle stability of rGO&Ni(OH)₂–Ni electrode maintaining 94.57% of its specific capacitance after 5000 cycles. The decrease is probably attributed to the phase transformation or the growth of particle and crystal

size of the electrode material during cycling process in alkali solution [57]. On the other hand, the ability of electrode material to retain high C_s at high discharge rate usually contributes to prominent energy and power characteristics. Ragone plot relating the energy density to power density is an efficient way to evaluate the capacitive performance of electrode material. The energy density (E , Wh kg⁻¹) and power density (P , W kg⁻¹) can be obtained from the following formulas:

$$E = \frac{1}{2} C_s (\Delta V)^2 \quad (2)$$

$$P = \frac{E}{t} \quad (3)$$

where C_s , and t are the specific capacitance (F g⁻¹), the potential range of a full discharge (V) and the time for a full discharge (s), respectively. Fig. S5 shows the Ragone plot of rGO&Ni(OH)₂–Ni derived from the GCD curves at different current densities. The rGO&Ni(OH)₂–Ni electrode displays an impressive energy density of 31.02 Wh kg⁻¹ at a power density of 224.98 W kg⁻¹. Although the energy density generally declines with the increase of power density, the energy density can still retain 20.25 Wh kg⁻¹ when the

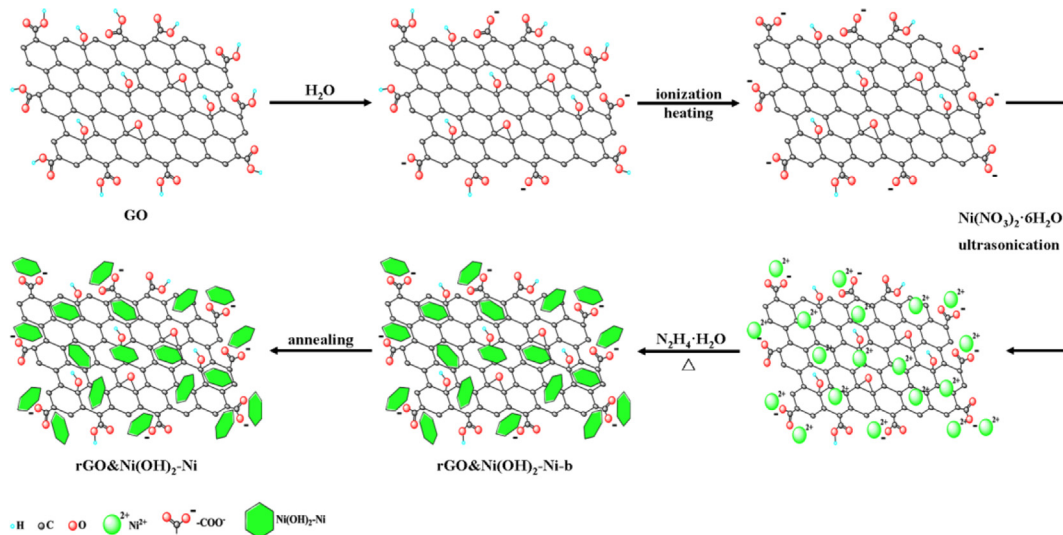


Fig. 7. Schematic of synthesis of rGO&Ni(OH)₂–Ni.

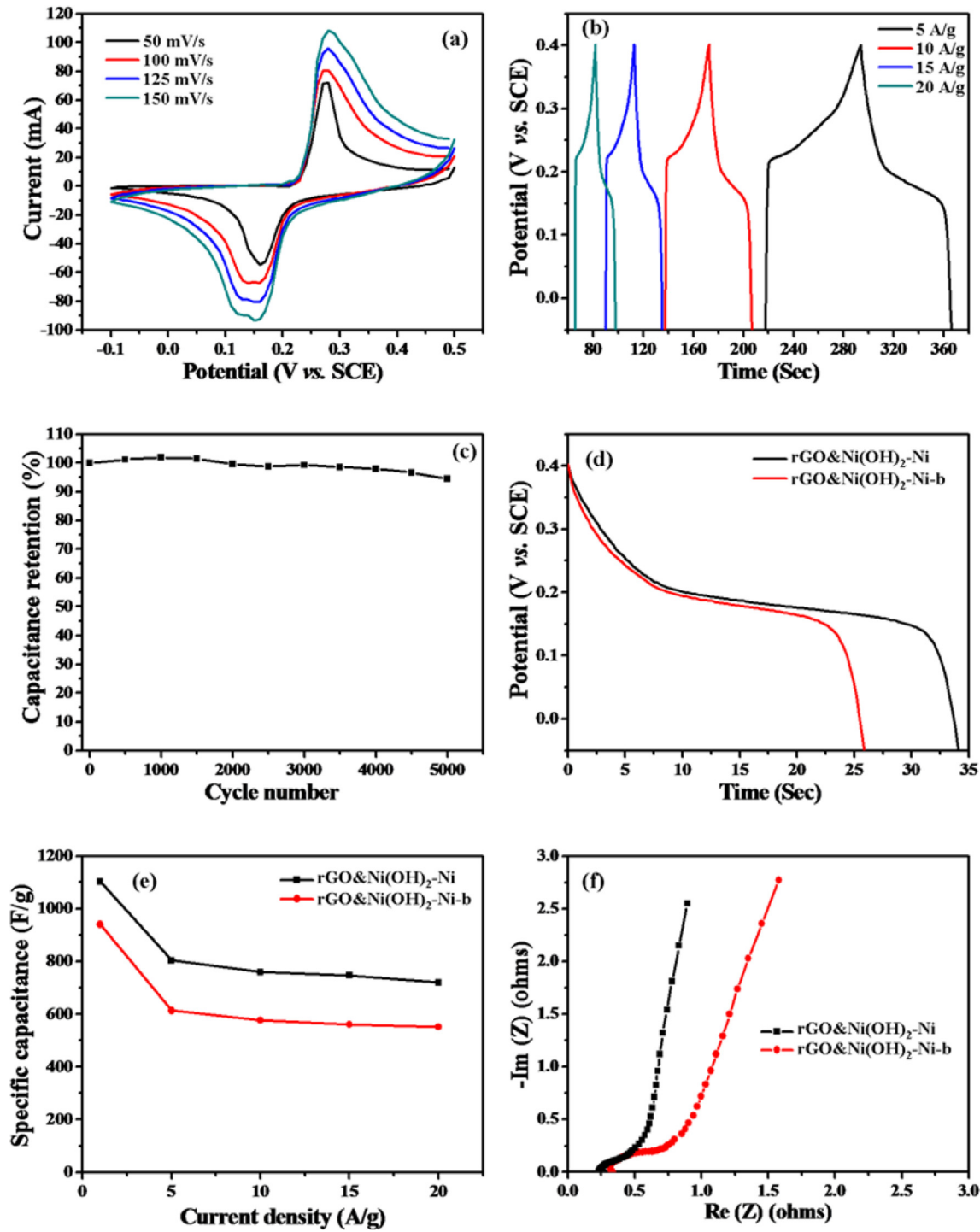


Fig. 8. (a) CV curves for rGO&Ni(OH)₂-Ni electrode at different scan rates. (b) GCD curves of rGO&Ni(OH)₂-Ni electrode collected at different current densities. (c) Cycle performance of rGO&Ni(OH)₂-Ni electrode measured at a scan rate of 100 mV s⁻¹. (d) Discharge curves of rGO&Ni(OH)₂-Ni-b and rGO&Ni(OH)₂-Ni at a current density of 10 A g⁻¹. (e) Specific capacitances of rGO&Ni(OH)₂-Ni-b and rGO&Ni(OH)₂-Ni measured as a function of current density. (f) Nyquist plots of rGO&Ni(OH)₂-Ni-b and rGO&Ni(OH)₂-Ni.

power density increases to 4500 W kg⁻¹, which is thanks to the excellent rate capability of rGO&Ni(OH)₂-Ni. High and stable energy density and power density suggest that the rGO&Ni(OH)₂-Ni is a highly promising candidate as supercapacitors electrode material for practical application.

The electrochemical testing results prove that the rGO&Ni(OH)₂-Ni owns significantly superior electrochemical performance, including high capacitance, high energy density,

excellent rate capability and good cycle stability, which is ascribed to the synergistic effect among Ni, Ni(OH)₂ and rGO. First, the nanoplates tightly contacted with the surface of rGO can effectively prevent the agglomeration of rGO, leading the excellent electrical property of rGO can be retained. Moreover, Ni combines with Ni(OH)₂ to form hexagonal morphology, so the electron and ion conduction can be enhanced due to the good conductivity of Ni. From these two aspects, the weakness of Ni(OH)₂ (poor electrical

Table 1

Summary of electrochemical data of some electrode materials. Complete data can be found in the related literatures.

Sample	Method	C_s (F g ⁻¹)	Electrolyte	Potential window (V)	Current density or scan rate	Ref.
Graphene/Ni(OH) ₂	Soft chemistry route	1087.9	6 M KOH	0.50	1.5 A g ⁻¹	[21]
Ni(OH) ₂ /graphene	Hydrothermal	1335	1 M KOH	0.50	2.8 A g ⁻¹	[15]
Ni(OH) ₂ /graphene	Microwave heating	523	6 M KOH	0.55	50 mV s ⁻¹	[50]
Graphene/Ni(OH) ₂	Solid-state reaction	820	1 M KOH	0.60	4 A g ⁻¹	[52]
Ni(OH) ₂ /graphene	Chemical precipitation	895	6 M KOH	0.55	20 mV s ⁻¹	[53]
rGO/Ni(OH) ₂	Non-aqueous approach	855	6 M KOH	0.45	10 mV s ⁻¹	[54]
Ni(OH) ₂ /MnO ₂	Surfactant-free	296.8	1 M Na ₂ SO ₄	1.00	1 A g ⁻¹	[55]
Ni(OH) ₂ /RGOCNT	Electrochemical	1235	6 M KOH	0.50	1 A g ⁻¹	[56]
Ni(OH) ₂ /CNTs	Chemical precipitation	432	6 M KOH	0.50	10 mV s ⁻¹	[19]
Ag@Ni(OH) ₂ /graphene	Hydrothermal	496	6 M KOH	0.50	1 A g ⁻¹	[31]
rGO&Ni(OH) ₂ –Ni	Chemical precipitation	1103	6 M KOH	0.45	1 A g ⁻¹	This work

conductivity) will be greatly overcome. What is more, the obtained hexagonal nanoplates can provide a short diffusion and migration pathway for electron and electrolyte ion and can increase the effective liquid–solid interfacial area, resulting in the effective electrochemical utilization of Ni(OH)₂. Given these advantages, the excellent electrochemical performance of rGO&Ni(OH)₂–Ni is entirely displayed. Thus, easy preparation and superior electrochemical property anticipate that rGO&Ni(OH)₂–Ni is a promising electrode material and has great potential application in supercapacitors.

3.5. Role of Ni (111) plane in electrochemical performance

In this work, interestingly, we find that Ni can improve not only the thermal stability of Ni(OH)₂, but also the electrochemical activity of composite due to the good electrical conductivity of Ni. It is well known that due to the anisotropy characteristic of crystal, different planes of crystal have different physical and chemical properties like electrical conductivity. Therefore, it is necessary to investigate the key plane in Ni for improving the electrochemical activity of composite. From the XRD results of rGO&Ni(OH)₂–Ni-b and rGO&Ni(OH)₂–Ni (Fig. 1(a,b)), we can find that after annealing treatment, the intensity of peak belonging to Ni (111) plane is increased while those belonging to Ni (200) plane and Ni (220) plane have no change. As mentioned above, this result indicates that the Ni (111) plane is promoted to grow after annealing treatment. Moreover, some works have pointed out that the (111) plane is one of the planes with preferential orientation in Ni [58]. In order to explore the influence of growth of Ni (111) plane on the electrochemical property of composite, the comparison of electrochemical performance between rGO&Ni(OH)₂–Ni-b and rGO&Ni(OH)₂–Ni is carried out. Fig. 8(d) displays the discharge curves of rGO&Ni(OH)₂–Ni-b and rGO&Ni(OH)₂–Ni at a current density of 10 A g⁻¹. Since the C_s value is proportional to the time for a full discharge (Eq. (1)), it is obvious that the C_s of rGO&Ni(OH)₂–Ni is higher than that of rGO&Ni(OH)₂–Ni-b. Besides, Fig. 8(e) presents the relationship between C_s and current density. As seen, the C_s values of rGO&Ni(OH)₂–Ni are all larger than those of rGO&Ni(OH)₂–Ni-b at various current densities. In addition, with the current density increases from 1 A g⁻¹ to 20 A g⁻¹, approximate 65.28% (720 F g⁻¹) of the initial capacitance (1103 F g⁻¹) for rGO&Ni(OH)₂–Ni is retained while only 58.55% (551 F g⁻¹) of the initial capacitance (941 F g⁻¹) for rGO&Ni(OH)₂–Ni-b is reserved, indicating higher capacitance retention ratio of rGO&Ni(OH)₂–Ni. These results demonstrate the better electrochemical property of rGO&Ni(OH)₂–Ni than that of rGO&Ni(OH)₂–Ni-b, which may be ascribed to the better electrical conductivity of Ni due to the growth of Ni (111) plane after annealing treatment, resulting in the better electrical conductivity of rGO&Ni(OH)₂–Ni.

To understand the electrochemical conductivity behaviors of rGO&Ni(OH)₂–Ni-b and rGO&Ni(OH)₂–Ni, EIS data are analyzed using Nyquist plots (Fig. 8(f)). Both of the plots start with semicircle loop followed by rising along imaginary impedance axis. First, the solution resistance can be considered as a series resistance of the electrolyte inside the pore and the interfacial resistance at the electroactive material/current collector and at the electrode/electrolyte interface. In the Nyquist plot, the equivalent series resistance (ESR) is represented as the intercept of real impedance axis. Obviously, the ESR value of rGO&Ni(OH)₂–Ni is lower than that of rGO&Ni(OH)₂–Ni-b, showing lower solution resistance of rGO&Ni(OH)₂–Ni. Second, the initial semicircle loop diameter indicates the charge transfer resistance and a larger diameter suggests more inhibition towards charge transfer. From the Nyquist plots, it can be seen that rGO&Ni(OH)₂–Ni has smaller semicircle loop diameter than rGO&Ni(OH)₂–Ni-b, implying faster charge transfer of rGO&Ni(OH)₂–Ni. Finally, the steeper line along the imaginary impedance axis indicates lower diffusion resistance. As seen, the line for rGO&Ni(OH)₂–Ni is steeper than that for rGO&Ni(OH)₂–Ni-b, demonstrating faster diffusion process of rGO&Ni(OH)₂–Ni. All these results prove that the rGO&Ni(OH)₂–Ni has better electrical conductivity than rGO&Ni(OH)₂–Ni-b. Thus, we can make a conclusion that the electrical conductivity of Ni is increased since (111) plane is grown after annealing treatment, which causes the improved electrical conductivity of rGO&Ni(OH)₂–Ni, resulting in the enhanced electrochemical activity. These results imply that the growth of Ni (111) plane plays a key role in Ni for further improving the electrochemical property of composite. More importantly, it is worthy noting that this discovery offers a new approach for using metal nanoparticle in improving the electrochemical performance of supercapacitor electrode material.

4. Conclusion

We have successfully prepared hexagonal Ni(OH)₂–Ni&rGO composite via easy one-step chemical precipitation method and subsequent annealing treatment. The results show that the thermal stability of Ni(OH)₂ is enhanced with the incorporation of Ni. Thanks to the positive synergistic effect among Ni, Ni(OH)₂ and rGO, the rGO&Ni(OH)₂–Ni electrode exhibits good stability at scan rates from 50 to 150 mV s⁻¹. A high specific capacitance of 1103 F g⁻¹ can be obtained at current density of 1 A g⁻¹ in 6 mol L⁻¹ KOH aqueous solution. With the current density increases from 1 to 20 A g⁻¹, the specific capacitance has low decay of 34.72% (from 1103 to 720 F g⁻¹), revealing excellent rate capability of rGO&Ni(OH)₂–Ni. A good energy density of 31.02 Wh kg⁻¹ has been obtained at a power density of 224.98 W kg⁻¹, and an energy density of 20.25 Wh kg⁻¹ can be still retained when the power density increases to 4500 W kg⁻¹. Moreover, the rGO&Ni(OH)₂–Ni

electrode shows a long cycle life, retaining 94.57% specific capacitance after 5000 cycles at scan rate of 100 mV s⁻¹. The advantages of easy preparation and remarkable electrochemical performance suggest the great potential application of rGO&Ni(OH)₂–Ni in supercapacitors. More importantly, our work finds that the Ni (111) plane is grown after annealing treatment, which plays a key role in Ni for further improving the electrochemical activity of composite. Such discovery will offer a new approach for using metal nanoparticle in improving the electrochemical property of supercapacitor electrode material.

Acknowledgments

The authors acknowledge financial support from the National Natural Science Foundation of China (51172099, 21006038 and 21376104), the Foundation of Science and Technology Projects of Guangdong Province (2011B090300018), the Fundamental Research Funds for the Central Universities (21612109), the Research and Innovation Project of Jinan University for Excellent Master (201321), and the 2013 Jinan University Challenge Cup for Student Extracurricular Academic Science and Technology Work Competition (201310B44).

Appendix A. Supplementary data

Supplementary data related to this article can be found at <http://dx.doi.org/10.1016/j.jpowsour.2014.05.106>.

References

- [1] P. Simon, Y. Gogotsi, *Nat. Mater.* 7 (2008) 845–854.
- [2] L.L. Zhang, X.S. Zhao, *Chem. Soc. Rev.* 38 (2009) 2520–2531.
- [3] A. Ghosh, Y.H. Lee, *ChemSusChem* 5 (2012) 480–499.
- [4] Z. Chen, V. Augustyn, J. Wen, Y. Zhang, M. Shen, B. Dunn, Y. Lu, *Adv. Mater.* 23 (2011) 791–795.
- [5] C. Liu, F. Li, L.-P. Ma, H.-M. Cheng, *Adv. Mater.* 22 (2010) E28–E62.
- [6] H. Jiang, L. Yang, C. Li, C. Yan, P.S. Lee, J. Ma, *Energy Environ. Sci.* 4 (2011) 1813–1819.
- [7] B.E. Conway, *Electrochemical Supercapacitors: Scientific Fundamentals and Technological Applications*, Kluwer Academic/Plenum Publisher, New York, 1999.
- [8] C.Z. Yuan, J.Y. Li, L.R. Hou, X.G. Zhang, L.F. Shen, X.W. Lou, *Adv. Funct. Mater.* 22 (2012) 4592–4597.
- [9] T. Brezesinski, J. Wang, S.H. Tolbert, B. Dunn, *Nat. Mater.* 9 (2010) 146–151.
- [10] S.G. Dai, Y. Xi, C.G. Hu, J.L. Liu, K.Y. Zhang, X.L. Yue, L. Cheng, *J. Mater. Chem. A* 1 (2013) 15530–15534.
- [11] J.P. Liu, J. Jiang, C.W. Cheng, H.X. Li, J.X. Zhang, H. Gong, H.J. Fan, *Adv. Mater.* 23 (2011) 2076–2081.
- [12] L.Q. Mai, F. Yang, Y.L. Zhao, X. Xu, L. Xu, Y.Z. Luo, *Nat. Commun.* 2 (2011).
- [13] X.H. Lu, M.H. Yu, T. Zhai, G.M. Wang, S.L. Xie, T.Y. Liu, C.L. Liang, Y.X. Tong, Y. Li, *Nano Lett.* 13 (2013) 2628–2633.
- [14] X.H. Lu, D.Z. Zheng, T. Zhai, Z.Q. Liu, Y.Y. Huang, S.L. Xie, Y.X. Tong, *Energy Environ. Sci.* 4 (2011) 2915–2921.
- [15] H.L. Wang, H.S. Casalongue, Y.Y. Liang, H.J. Dai, *J. Am. Chem. Soc.* 132 (2010) 7472–7477.
- [16] J.W. Lang, L.B. Kong, W.J. Wu, M. Liu, Y.C. Luo, L. Kang, *J. Solid State Electr.* 13 (2009) 333–340.
- [17] Y.M. Ren, L. Wang, Z.J. Dai, X.K. Huang, J.J. Li, N. Chen, J. Gao, H.L. Zhao, X.M. Sun, X.M. He, *Int. J. Electrochem. Sci.* 7 (2012) 12236–12243.
- [18] Z.P. Cheng, J.M. Xu, H. Zhong, D. Li, P.C. Zhu, Y. Yang, *Superlattices Microstruct.* 48 (2010) 154–161.
- [19] C.G. Liu, Y.S. Lee, Y.J. Kim, I.C. Song, J.H. Kim, *Synth. Met.* 159 (2009) 2009–2012.
- [20] D.L. Fang, Z.D. Chen, X. Liu, Z.F. Wu, C.H. Zheng, *Electrochim. Acta* 81 (2012) 321–329.
- [21] J.W. Zhu, S. Chen, H. Zhou, X. Wang, *Nano Res.* 5 (2012) 11–19.
- [22] J. Zhang, L.B. Kong, J.J. Cai, H. Li, Y.C. Luo, L. Kang, *Micropor. Mesopor. Mat.* 132 (2010) 154–162.
- [23] A.K. Geim, K.S. Novoselov, *Nat. Mater.* 6 (2007) 183–191.
- [24] M.J. Allen, V.C. Tung, R.B. Kaner, *Chem. Rev.* 110 (2010) 132–145.
- [25] D.A.C. Brownson, D.K. Kampouris, C.E. Banks, *Chem. Soc. Rev.* 41 (2012) 6944–6976.
- [26] Y. Huang, J.J. Liang, Y.S. Chen, *Small* 8 (2012) 1805–1834.
- [27] G.P. Wang, L. Zhang, J. Kim, J.J. Zhang, *J. Power Sources* 217 (2012) 554–561.
- [28] Z. You, K. Shen, Z.C. Wu, X.F. Wang, X.H. Kong, *Appl. Surf. Sci.* 258 (2012) 8117–8123.
- [29] J.W. Lang, L.B. Kong, M. Liu, Y.C. Luo, L. Kang, *J. Solid State Electr.* 14 (2010) 1533–1539.
- [30] J.H. Zhong, A.L. Wang, G.R. Li, J.W. Wang, Y.N. Ou, Y.X. Tong, *J. Mater. Chem.* 22 (2012) 5656–5665.
- [31] D. Ghosh, S. Giri, A. Mandal, C.K. Das, *Chem. Phys. Lett.* 573 (2013) 41–47.
- [32] W.S. Hummers Jr., R.E. Offeman, *J. Am. Chem. Soc.* 80 (1958) 1339.
- [33] N.I. Kovtyukhova, P.J. Ollivier, B.R. Martin, T.E. Mallouk, S.A. Chizik, E.V. Buzaneva, A.D. Gorchinskii, *Chem. Mater.* 11 (1999) 771–778.
- [34] D.H. Deng, X.L. Pan, L.A. Yu, Y. Cui, Y.P. Jiang, J. Qi, W.X. Li, Q.A. Fu, X.C. Ma, Q.K. Xue, G.Q. Sun, X.H. Bao, *Chem. Mater.* 23 (2011) 1188–1193.
- [35] B.J. Li, H.Q. Cao, J. Shao, H. Zheng, Y.X. Lu, J.F. Yin, M.Z. Qu, *Chem. Commun.* 47 (2011) 3159–3161.
- [36] H. Chai, X. Chen, D. Jia, S. Bao, W. Zhou, *Mater. Res. Bull.* 47 (2012) 3947–3951.
- [37] X.M. Liu, X.G. Zhang, S.Y. Fu, *Mater. Res. Bull.* 41 (2006) 620–627.
- [38] S.-G. Hwang, G.-O. Kim, S.-R. Yun, K.-S. Ryu, *Electrochim. Acta* 78 (2012) 406–411.
- [39] V. Datsyuk, M. Kalyva, K. Papagelis, J. Parthenios, D. Tasis, A. Siokou, I. Kallitsis, C. Gallois, *Carbon* 46 (2008) 833–840.
- [40] S. Park, J.H. An, I.W. Jung, R.D. Piner, S.J. An, X.S. Li, A. Velamakanni, R.S. Ruoff, *Nano Lett.* 9 (2009) 1593–1597.
- [41] I.G. Casella, M.R. Guascito, M.G. Sannazzaro, *J. Electroanal. Chem.* 462 (1999) 202–210.
- [42] A.P. Grosvenor, M.C. Biesinger, R.S. Smart, N.S. McIntyre, *Surf. Sci.* 600 (2006) 1771–1779.
- [43] H.K. Jeong, Y.P. Lee, R.J.W.E. Lahaye, M.H. Park, K.H. An, I.J. Kim, C.W. Yang, C.Y. Park, R.S. Ruoff, Y.H. Lee, *J. Am. Chem. Soc.* 130 (2008) 1362–1366.
- [44] H.L. Guo, X.F. Wang, Q.Y. Qian, F.B. Wang, X.H. Xia, *ACS Nano* 3 (2009) 2653–2659.
- [45] X.M. Ni, Q.B. Zhao, B.B. Li, J. Cheng, H.G. Zheng, *Solid State Commun.* 137 (2006) 585–588.
- [46] L.X. Yang, Y.J. Zhu, H. Tong, Z.H. Liang, L. Li, L. Zhang, *J. Solid State Chem.* 180 (2007) 2095–2101.
- [47] F. Liu, X. Zhang, K.W. Zhu, Y. Song, Z.H. Shi, B.X. Feng, *J. Mater. Sci.* 44 (2009) 6028–6034.
- [48] K.R. Raj, G. Bhagavannarayana, P. Murugakoothan, *Optik* 124 (2013) 493–500.
- [49] S.H. Wu, D.H. Chen, *J. Colloid Interf. Sci.* 259 (2003) 282–286.
- [50] J. Yan, Z.J. Fan, W. Sun, G.Q. Ning, T. Wei, Q. Zhang, R.F. Zhang, L.J. Zhi, F. Wei, *Adv. Funct. Mater.* 22 (2012) 2632–2641.
- [51] F.S. Cai, G.Y. Zhang, J. Chen, X.L. Gou, H.K. Liu, S.X. Dou, *Angew. Chem. Int. Ed.* 43 (2004) 4212–4216.
- [52] Z. Sun, X. Lu, *Ind. Eng. Chem. Res.* 51 (2012) 9973–9979.
- [53] J. Yan, W. Sun, T. Wei, Q. Zhang, Z. Fan, F. Wei, *J. Mater. Chem.* 22 (2012) 11494–11502.
- [54] J.W. Lee, T. Ahn, D. Soundararajan, J.M. Ko, J.-D. Kim, *Chem. Commun.* 47 (2011) 6305–6307.
- [55] H. Jiang, C.Z. Li, T. Sun, J. Ma, *Chem. Commun.* 48 (2012) 2606–2608.
- [56] L.L. Zhang, Z.G. Xiong, X.S. Zhao, *J. Power Sources* 222 (2013) 326–332.
- [57] G.X. Hu, C.X. Li, H. Gong, *J. Power Sources* 195 (2010) 6977–6981.
- [58] A. Cortes, G. Riveros, J.C. Denardin, R.E. Marotti, E.A. Dalchiele, H. Gomez, J. Nanosci. Nanotechnol. 9 (2009) 1992–2000.

Glossary

- GO: graphene oxide
 rGO: reduced graphene oxide
 XRD: X-ray diffraction
 FTIR: fourier transform infrared
 XPS: X-ray photoelectron spectroscopy
 TGA: thermogravimetric analysis
 EDX: energy dispersive X-ray spectrometer
 FESEM: field emission scanning electron microscopy
 TEM: transmission electron microscopy
 SCE: saturated calomel electrode
 CV: cyclic voltammetry
 GCD: galvanostatic charge and discharge
 EIS: electrochemical impedance spectroscopy
 C_s: specific capacitance
 I: discharge current
 t: time for a full discharge
 m: mass of electroactive material
 ΔV: potential range of a full discharge
 E: energy density
 P: power density
 ESR: equivalent series resistance